

# Spin-orbit microlaser emitting in a four-dimensional Hilbert space

Zhifeng Zhang,<sup>1,2,8</sup> Haoqi Zhao,<sup>2,8</sup> Shuang Wu,<sup>1</sup> Tianwei Wu,<sup>1</sup> Xingdu Qiao,<sup>2</sup> Zihe Gao,<sup>1</sup> Ritesh Agarwal,<sup>1</sup> Stefano Longhi,<sup>3,4</sup> Natalia M. Litchinitser,<sup>5</sup> Li Ge,<sup>6,7</sup> Liang Feng<sup>1,2\*</sup>

<sup>1</sup>*Department of Materials Science and Engineering, University of Pennsylvania, Philadelphia, PA 19104, USA*

<sup>2</sup>*Department of Electrical and Systems Engineering, University of Pennsylvania, Philadelphia, PA 19104, USA*

<sup>3</sup>*Dipartimento di Fisica, Politecnico di Milano, Piazza L. da Vinci 32, Milano I-20133, Italy*

<sup>4</sup>*IFISC (UIB-CSIC), Instituto de Fisica Interdisciplinar y Sistemas Complejos, Palma de Mallorca, Spain*

<sup>5</sup>*Department of Electrical and Computer Engineering and Department of Physics, Duke University, Durham, NC 27708, USA*

<sup>6</sup>*Department of Engineering Science and Physics, College of Staten Island, CUNY, Staten Island, NY 10314, USA*

<sup>7</sup>*The Graduate Center, CUNY, New York, NY 10016, USA*

<sup>8</sup>*These authors contributed equally: Zhifeng Zhang, Haoqi Zhao*

\*Corresponding author: [fenglia@seas.upenn.edu](mailto:fenglia@seas.upenn.edu)

**A step toward the next generation of high-capacity, noise-resilient communication and computing technologies is a significant increase in the dimensionality of information space and the synthesis of superposition states on an  $N$ -dimensional ( $N > 2$ ) Hilbert space featuring exotic group symmetries. Despite the rapid development of photonic devices and systems, on-chip information technologies are mostly limited to two-level systems due to the lack of sufficient reconfigurability to satisfy the stringent requirement for  $2(N - 1)$  degrees of freedom, intrinsically associated with the increase of synthetic dimensionalities. Even with extensive efforts dedicated to recently emerged vector lasers and micro-cavities for the expansion of dimensionalities<sup>1-10</sup>, it still remains a grand challenge to actively tune the diversified, high-dimensional superposition states of light on demand. Here, we demonstrate a hyperdimensional, spin-orbit microlaser for chip-scale flexible generation and**

**manipulation of arbitrary four-level states. Two microcavities coupled through a non-Hermitian synthetic gauge field are designed to emit spin-orbit-coupled states of light with six degrees of freedom (DOF). The vectorial state of the emitted laser beam in free space can be mapped on a Bloch hypersphere defining an SU(4) symmetry, demonstrating dynamical generation and reconfiguration of high-dimensional superposition states with high fidelity.**

## **Main**

Information systems today are built upon binary digits (i.e., bits), taking two possible values: 0 or 1. When dealing with a quantum bit or its classical analogue, any arbitrary coherent superposition of them is allowed. Such binary representations can be equivalently translated to a two-level system, where the dynamical evolution and manipulation of the state are conveniently described on a Bloch (or Poincaré) sphere using the SU(2) algebra<sup>11,12</sup>. With the continuously growing demand for increased information density and security, there is a necessity for constructing and exploring a larger Hilbert space towards a generic  $N$ -level system, realizing effective control on a higher-dimensional Bloch hypersphere (an extension of a Bloch sphere for an arbitrary  $N$ -level system)<sup>13,14</sup>. For example, the SU(4) group represents unitary operations in a four-level system where four eigen bases form a four-dimensional (4D) Hilbert space (see Supplementary Information section 1). An arbitrary state in it is the superposition of these eigen bases with four complex coefficients, and the increased dimensionality enables superdense coding, signal fidelity, and accelerated computation with reduced complexity and increased algorithm efficiency<sup>15-19</sup>. Although similar mathematical frameworks are being formulated for the SU( $N$ ) symmetry<sup>14,20</sup>, their experimental demonstration has not been realized to date in contrast to the two-level system, especially for free space, long-haul communications. One major challenge is to gain full control of the  $2(N - 1)$  DOFs required by a generic  $N$ -level pure state  $|\Psi\rangle$ .

Optical beams carrying spin angular momentum provide an important class of two-level systems, which can be represented on a standard Bloch sphere<sup>12</sup>. Here, the two pole states correspond to orthogonal polarizations, while the rest of the sphere covers all other possible polarization states of light, with the unitary operators connecting them via the SU(2) group. Spatial modes, in addition to polarization, offer a promising route to high-dimensional Hilbert spaces<sup>21</sup> with the mathematical framework generalized from the conventional spin Bloch sphere to the spin-orbit high-order Poincaré sphere (HOPS), by incorporating both spin ( $s$ ) and orbital angular

momenta (OAM:  $l$ ) of light<sup>22-25</sup>. The complex optical fields described by the HOPS are non-separable states (except at the poles) with respect to spin and OAM, and hence important in promoting scalar OAM beams to a more general type of spin-orbit vectorial states, enhancing the spectral efficiency for a high-capacity communication network<sup>26-28</sup>. Although manipulating spin-orbit vectorial states of light can in principle generate a 4D Hilbert space and its SU(4) algebra, a single HOPS achieved so far is still limited to the SU(2) algebra as a subspace of a four-level system<sup>14,23</sup>.

Here, we demonstrate a fully integrated semiconductor microlaser exploiting spin-orbit coupling of light to drastically expand the DOFs as compared to the state-of-the-art<sup>1-9</sup>. Tunable asymmetric couplings enabled by a synthetic imaginary gauge field<sup>1,29-31</sup> provide flexible control of up to six DOFs, thus enabling the full coverage of a 4D Hilbert space. We show versatile spin-orbit-coupled beam emission control, demonstrate the precise generation and arbitrary reconfiguration of high-dimensional superposition states, and characterize the vectorial coherence of laser emission mapped on the Bloch hypersphere defined by the SU(4) algebra.

### Design of the hyperdimensional microlaser

The hyperdimensional microlaser, emitting in a 4D Hilbert space, consists of two same-sized microrings fabricated on a III-V semiconductor platform with 200 nm thick InGaAsP multiple quantum wells. The microrings are coupled through an imaginary gauge formed by four control waveguides, which are themselves connected using two 3-dB directional couplers (Fig. 1a and Fig. 1b). Each microring intrinsically supports two degenerate modes (clockwise (CW) and counterclockwise (CCW)) at our target frequency. Therefore, it effectively features an SU(2) group, and the entire laser can be viewed as a four-level system described by the following Hamiltonian:

$$H = \begin{bmatrix} \omega_{cw,II} + ig_i + g_r & 0 & -ike^{g_1+g_3+i(\varphi_1+\varphi_3)} & -ke^{g_2+g_3+i(\varphi_2+\varphi_3)} \\ 0 & \omega_{ccw,II} + ig_i + g_r & ke^{g_1+g_4+i(\varphi_1+\varphi_4)} & -ike^{g_2+g_4+i(\varphi_2+\varphi_4)} \\ -ike^{g_2+g_4+i(\varphi_2+\varphi_4)} & -ke^{g_2+g_3+i(\varphi_2+\varphi_3)} & \omega_{cw,I} - ig_i - g_r & 0 \\ ke^{g_1+g_4+i(\varphi_1+\varphi_4)} & -ike^{g_1+g_3+i(\varphi_1+\varphi_3)} & 0 & \omega_{ccw,I} - ig_i - g_r \end{bmatrix}. \quad (1)$$

Here,  $\omega_{cw,I}$ ,  $\omega_{ccw,I}$ ,  $\omega_{cw,II}$ , and  $\omega_{ccw,II}$  are the resonant frequencies of four degenerate modes in the two microring resonators, with the subscripts denoting their chirality (CW and CCW) and location (**I**, left, and **II**, right);  $g_r$  and  $ig_i$  denote the real frequency detuning and the gain-loss contrast between the two microring resonators, respectively;  $k$  represents the effective coupling

strength between the two microrings;  $g_{1-4}$  corresponds to the single pass amplification/attenuation through control waveguides 1-4, respectively, while  $\varphi_{1-4}$  is the accumulated phase when light propagates through each control waveguide. Although the CW and CCW modes in the same microring do not couple with each other directly, they interact through both modes in the other microring resonator. The fundamental eigenmode of the microlaser can be described as  $|\Psi\rangle = [E_{II} \ rE_I]^T$ , where  $E_I = [E_{cw,I} \ E_{ccw,I}]^T = [-ie^{-\frac{g_1-g_2}{2}-i\frac{\varphi_1-\varphi_2}{2}} \ e^{\frac{g_1-g_2}{2}+i\frac{\varphi_1-\varphi_2}{2}}]^T$  and  $E_{II} = [E_{cw,II} \ E_{ccw,II}]^T = [-ie^{\frac{g_3-g_4}{2}+i\frac{\varphi_3-\varphi_4}{2}} \ e^{-\frac{g_3-g_4}{2}-i\frac{\varphi_3-\varphi_4}{2}}]^T$  are the eigenvectors in the left and right microrings, respectively, where  $r = \frac{\sqrt{g'^2+\eta^2}+g'}{\eta}$  with  $g' = (g_i - ig_r)/2k$  and  $\eta = e^{\sum_j(g_j+i\varphi_j)/2}$  (see Supplementary Information section 2). It is therefore evident that selective pumping and phase tuning of the control waveguides quantify four DOFs necessary for individual control of two SU(2) groups:  $g_1 - g_2$  and  $\varphi_1 - \varphi_2$  for the control of the chirality and phase in the left ring, whereas  $g_3 - g_4$  and  $\varphi_3 - \varphi_4$  for the right ring. Additionally, the amplitude and phase of  $r$ , which can be controlled, for example, by  $g_r$  and  $g_i$ , provide two additional DOFs to realize a full 4D Hilbert space.

To elucidate the SU(4) property of this microlaser, we introduce three HOPSs with a total of six DOFs. Each HOPS features a north pole state  $|N\rangle$  and a south pole state  $|S\rangle$ , and their amplitude ratio and relative phase are represented by the latitude  $\theta$  and longitude  $\phi$  on the HOPS, respectively:

$$|\Psi(\theta, \phi)\rangle = \cos(\theta/2) e^{-i\phi/2}|N\rangle + \sin(\theta/2) e^{i\phi/2}|S\rangle. \quad (2)$$

Below, we use HOPS **I** to depict the left ring with  $|N_I\rangle = | + 2, \uparrow\rangle$  and  $|S_I\rangle = | - 2, \downarrow\rangle$ , whereas HOPS **II** represents the right ring with  $|N_{II}\rangle = | - 2, \uparrow\rangle$  and  $|S_{II}\rangle = | + 2, \downarrow\rangle$ , where we carefully design the microring cavities to generate the desired pole states and enable the spin-orbit locking:  $|N_I\rangle$  and  $|S_I\rangle$  are translated from CW and CCW modes of left ring, and so do  $|N_{II}\rangle$  and  $|S_{II}\rangle$  for the right ring (see Methods). Note that these four spin-orbit-coupled states overlap completely in both space and time and share the same diffraction and modal conversion (from free space to fibers and vice versa), so these states can maintain their coherence after long-distance propagation, which is critical for long-haul communications. The SU(4) hypersphere is completed by HOPS **III**. Its north (south) pole state can be arbitrarily chosen on HOPS **II** (**I**) (Fig. 1a). Note that the coupling of HOPS **I** and **II** on HOPS **III**, while each representing a distinct SU(2) group, enables the generation of the high-dimensional superposition states that cover the entire 4D Hilbert space.

With the full control over the six DOFs discussed above, the tuning operations involved contain a representation of the SU(4) group (see Supplementary Information section 1).

### Manipulation on SU(4) Bloch hypersphere

One prominent feature of our system is that these three HOPSSs can be independently controlled. Here, we first focus on HOPS **I** and **II**. In the lasing mode,  $g_1 - g_2$  and  $\varphi_1 - \varphi_2$  determine the latitude and longitude on HOPS **I**, and so do  $g_3 - g_4$  and  $\varphi_3 - \varphi_4$  on HOPS **II**. These two HOPSSs can be selectively characterized while the entire microlaser is pumped (including the control waveguides to maintain the non-Hermitian-controlled gauge): the emission from one of them is collected and analyzed, one at a time. The gain and phase accumulation in each control waveguide can be individually tuned by selective optical pumping, using a nanosecond laser, and heating, using a continuous-wave laser, both at the wavelength of 1064 nm (see Methods). For example, by applying equal optical pumping of the nanosecond laser to waveguides 1 and 2 (i.e.,  $g_1 = g_2$ ), the spin-orbit state of laser emission from the left microring contains equally weighted  $|N_l\rangle$  and  $|S_l\rangle$  and is thus confined along the equator of HOPS **I**. To manipulate the state in the azimuthal direction, heating pads 1 and 2 (Fig. 1a) are selectively excited, where the local temperature increase mainly induces the phase accumulation in their adjacent waveguides (i.e.,  $\varphi_1$  and  $\varphi_2$ , respectively). By varying the heating powers on the two heating pads, the relative phase  $\varphi_2 - \varphi_1$  can be swept from 0 to  $2\pi$ , enabling the full phase control along the longitude of HOPS **I** (Fig. 2a). Non-separability intrinsically associated with spin-orbit-coupled vectorial states is validated by placing a horizontally polarized linear polarizer in the optical path. The intensity patterns collected after the linear polarizer show 4 lobes in the azimuthal direction, resulting from the interference of equally weighted OAM orders of  $\pm 2$ ; these patterns rotate as a function of  $(\varphi_2 - \varphi_1)/4$ , and the relative phase between the two OAM orders manifests an  $8\pi$  winding measured using Stokes polarimetry<sup>32</sup> (see Methods). Similar phase control can be independently carried out on HOPS **II** in the right microring (Fig. 2b), using heaters 3 and 4 to maneuver  $\varphi_3 - \varphi_4$  in waveguides 3 and 4. The orientation of the 4 lobes rotates in the opposite azimuthal direction because now the north pole state has  $l = -2$  instead of  $l = 2$ .

To reconfigure the state along the latitude of HOPS **I** and **II**, selective pumping of the nanosecond laser is projected onto the control waveguides to tune their amplification/attenuation rates (e.g.,  $g_1 - g_2$  for the left microring), and thus, the power ratio between two pole states, as

suggested by the definition of  $\theta$ . Five special states are produced along the latitude at  $\phi = 0$  on HOPS **I** with an equal spacing of  $\pi/2$  ( $P_{5,9}$  in Fig. 2c), where the intensities of the two spin components reveal the evolution of the ratio between  $|N_I\rangle = | + 2, \uparrow \rangle$  and  $|S_I\rangle = | - 2, \downarrow \rangle$ , corresponding to the evolution of the resonant mode in the left microring from purely CCW to purely CW. Similar chiral control can be independently performed in the right microring, by manipulating the state along the latitude of HOPS **II** from  $|N_{II}\rangle = | - 2, \uparrow \rangle$  to  $|S_{II}\rangle = | + 2, \downarrow \rangle$  (Fig. 2d).

To complete the state control on the SU(4) Bloch hypersphere, below we detail the maneuver on HOPS **III**, arising from the superposition of vectorial states on HOPS **I** and **II** (Fig. 3a)<sup>14</sup>: As aforementioned, their relative amplitude and phase between two vector beams can be controlled inherently via  $g_i$  and  $g_r$  in Eq. (1), which *do not* affect HOPS **I** and **II**. The gain/loss contrast  $g_i$  between the two microrings can be precisely controlled by projecting different pump powers onto them. Its dominant effect is tuning the latitude on HOPS **III**, as can be seen from the continuous variation of emission power chirality from two rings (Fig. 3b). Phase tuning on HOPS **III** is accomplished with the onsite frequency detuning between two microrings (i.e.,  $g_r$ ), by selectively heating pad 5 or 6 (Fig. 1) to create a temperature gradient in the horizontal direction across the microlaser. Although this procedure may also alter the refractive index of the control waveguides, and in turn, the phase accumulation in each waveguide (i.e.,  $\varphi_i$ ),  $\varphi_2 - \varphi_1$  and  $\varphi_3 - \varphi_4$  remain unchanged due to the placements of these two heating pads. Therefore, HOPS **I** and **II** are not affected when we move the states on HOPS **III**. To demonstrate phase control between two microrings, two experiments under different settings are conducted. In both cases, heating pad 5 is pumped using the continuous-wave laser with precisely controlled power, and we choose states at  $\phi = 0$  on both HOPS **I** and **II**. The phase difference between two microrings is extracted by analyzing the far field emission patterns (see Supplementary Information section 3). In the first case, the left microring is dominated by the CCW mode ( $\theta \approx 0.11\pi$  on HOPS **I**), while both CW and CCW modes exist in the right microring ( $\theta \approx 0.70\pi$  on HOPS **II**). The phase difference versus heating laser power is plotted in Fig. 3c, showing nearly linear phase tuning in a full  $2\pi$  range. In the second case, CW and CCW modes coexist in both microrings ( $\theta \approx 0.44\pi$  and  $0.54\pi$  on HOPS **I** and **II**, respectively), and  $\pi$  phase jumps are observed in experiments, as shown in Fig. 3d, which could be explained by supermode-hopping during the power heating scan. Note that compared with theoretical predictions based on Eq. (1), our experimental system revealed richer dynamics

so a wider tuning range of the longitude on HOPS **III** was observed in experiments (see Supplementary Information section 2). This deviation, which might be ascribable to a heating-induced more complex and simultaneous change of parameters in the Hamiltonian, suggests the limitations of our linear model.

The ability to map the vectorial states on the SU(4) Bloch hypersphere enables the generation and reconfiguration of intriguing higher-dimensional states (see Supplementary Videos) that are resilient to noise, and therefore, important in computations and communications for error corrections<sup>33</sup>. Fig. 4 demonstrates the generation and reconfiguration between two iconic states using our hyperdimensional microlaser:  $|\psi_1\rangle = \frac{1}{2}(|+2, \uparrow\rangle + |-2, \downarrow\rangle + |-2, \uparrow\rangle - |+2, \downarrow\rangle)$ , a spin-orbit high-dimensional superposition state corresponding to the in-phase superposition of state P1 on HOPS **I** (Fig. 2a) and state P3 on HOPS **II** (Fig. 2B); and  $|\psi_2\rangle = \frac{\sqrt{2}}{2}(|+2, \uparrow\rangle - |-2, \uparrow\rangle)$ , a non-vectorial state representing the out-of-phase superposition of P5 on HOPS **I** (Fig. 2c) and P5 on HOPS **II** (Fig. 2d). In the far field, while the two vector beams overlap perfectly in size and geometry, interference fringes arise as a result of their slightly different emission angles, which experimentally facilitates the retrieval and analysis of only the cross-correlated term (see Supplementary Information section 3). This property allows us to confirm spatially inhomogeneous and vectorial characteristics of the superposition state: For state  $|\psi_1\rangle$ , opposite polarization windings from the two rings (see the phase winding maps in Figs. 2a and 2b) yield a cross-correlation pattern with 8 lobes in the far field with their phase alternatingly quantized at either 0 or  $\pi$  (Figs. 4a and 4b), where high/low intensity denotes aligned/orthogonal polarizations, respectively. Furthermore, the experimentally measured density matrix shows high fidelity of 0.998, consistent with the calculated result (Fig. 4c and Fig. 4d) (see Supplementary Information section 4). Dynamical reconfiguration of selective pumping can swiftly transform laser emission from  $|\psi_1\rangle$  to  $|\psi_2\rangle$ . The two eigen-states in  $|\psi_2\rangle$  possess the same polarization, therefore leading to a cross-correlation pattern with uniform intensity in the far field and a continuous phase winding of  $8\pi$  in the azimuthal direction (Figs. 4e and 4f). The phase winding arises from the phase difference associated with opposite OAM orders of  $\pm 2$ . The experimentally retrieved density matrix also agrees well with theoretical calculations, showing high fidelity of 0.942 (Figs. 4g and 4h).

## Conclusion

We have demonstrated a non-Hermitian-controlled spin-orbit microlaser, whose emitted beams are intrinsically spatially inhomogeneous and possess six DOFs, allowing for the arbitrary generation and dynamical reconfiguration of intriguing high-dimensional superposition states with high fidelity. Although the current linear model provides a glimpse into the rich dynamics of our microlaser system, it is important to continue developing a more comprehensive model that takes into account various thermal and optical nonlinearities for better control of the superposition state in the 4D Hilbert space. While being classical, such high-dimensional superposition states, when attenuated to the single photon level, can be applied to perform well-established decoy state protocols<sup>34</sup> for high-dimensional quantum key distribution with a higher security key rate<sup>35</sup>. Additionally, intrinsic spin-orbit non-separability associated with the high-dimensional superposition state features high-dimensional non-separable states with the potential to further promote the precision limit in metrology, imaging, and information science<sup>36-39</sup>. The carefully selected four spin-orbit-coupled states possess the same propagation properties and completely overlap in both space and time, thereby maintaining long-distance coherence that is ideal for free space quantum communication. Complementary to the previously demonstrated  $N$ -mode Hilbert space using integrated circuits (where high-dimensionality, represented as superposition states of waveguide modes, is limited on-chip)<sup>40</sup>, our hyperdimensional microlaser provides an integrated solution for the deployment of next generation high-capacity, noise-resilient communication technologies.



## References:

1. Zhang, Z. et al. Tunable topological charge vortex microlaser. *Science* **368**, 760-763 (2020).
2. Shao, Z., Zhu, J., Chen, Y., Zhang, Y. & Yu, S. Spin-orbit interaction of light induced by transverse spin angular momentum engineering. *Nat. Commun.* **9**, 1-11 (2018).
3. Qiao, X. et al. Higher-dimensional supersymmetric microlaser arrays. *Science* **372**, 403-408 (2021).
4. Ma, X. et al. High-speed directly modulated cylindrical vector beam lasers. *ACS Photonics* **6**, 3261-3270 (2019).
5. Papič, M. et al. Topological liquid crystal superstructures as structured light lasers. *Proc. Natl Acad. Sci. USA* **118**, e2110839118 (2021).
6. Komisar, D., Kumar, S., Kan, Y., Wu, C. & Bozhevolnyi, S. I. Generation of radially polarized single photons with plasmonic bullseye antennas. *ACS Photonics* **8**, 2190-2196 (2021).
7. Lin, W., Ota, Y., Arakawa, Y. & Iwamoto, S. Microcavity-based generation of full Poincaré beams with arbitrary skyrmion numbers. *Phys. Rev. Res.* **3**, 023055 (2021).
8. Mohamed, S. et al. Controlling Topology and Polarization State of Lasing Photonic Bound States in Continuum. *Laser Photon. Rev.*, 2100574 (2022).
9. He, C., Shen, Y. & Forbes, A. Towards higher-dimensional structured light. *Light Sci. Appl.* **11**, 1-17 (2022).
10. Miao, P. et al. Orbital angular momentum microlaser. *Science* **353**, 464-467 (2016).
11. Bloch, F. Nuclear induction. *Phys. Rev.* **70**, 460 (1946).
12. Padgett, M. J. & Courtial, J. Poincaré-sphere equivalent for light beams containing orbital angular momentum. *Opt. Lett.* **24**, 430-432 (1999).
13. Kimura, G. The Bloch vector for N-level systems. *Phys. Lett. A* **314**, 339-349 (2003).

14. Kemp, C. J., Cooper, N. R. & Ünal, F. N. Nested-sphere description of the N-level Chern number and the generalized Bloch hypersphere. *Phys. Rev. Res.* **4**, 023120 (2022).
15. Barreiro, J. T., Wei, T.-C. & Kwiat, P. G. Beating the channel capacity limit for linear photonic superdense coding. *Nat. Phys.* **4**, 282-286 (2008).
16. Bouchard, F., Fickler, R., Boyd, R. W. & Karimi, E. High-dimensional quantum cloning and applications to quantum hacking. *Sci. Adv.* **3**, e1601915 (2017).
17. Wang, Y., Hu, Z., Sanders, B. C. & Kais, S. Qudits and high-dimensional quantum computing. *Front. Phys.* **8**, 589504 (2020).
18. Gao, X., Erhard, M., Zeilinger, A. & Krenn, M. Computer-inspired concept for high-dimensional multipartite quantum gates. *Phys. Rev. Lett.* **125**, 050501 (2020).
19. Wang, F. et al. Generation of the complete four-dimensional Bell basis. *Optica* **4**, 1462-1467 (2017).
20. Tilma, T., Byrd, M. & Sudarshan, E. A parametrization of bipartite systems based on SU(4) Euler angles. *J. Phys. A Math. Gen.* **35**, 10445 (2002).
21. Forbes, A. & Nape, I. Quantum mechanics with patterns of light: Progress in high dimensional and multidimensional entanglement with structured light. *AVS Quantum Sci.* **1**, 011701 (2019).
22. Milione, G., Sztul, H., Nolan, D. & Alfano, R. Higher-order Poincaré sphere, Stokes parameters, and the angular momentum of light. *Phys. Rev. Lett.* **107**, 053601 (2011).
23. Naidoo, D. et al. Controlled generation of higher-order Poincaré sphere beams from a laser. *Nat. Photon.* **10**, 327-332 (2016).
24. Shen, Y., Yang, X., Naidoo, D., Fu, X. & Forbes, A. Structured ray-wave vector vortex beams in multiple degrees of freedom from a laser. *Optica* **7**, 820-831 (2020).

25. Shen, Y. et al. Creation and control of high-dimensional multi-partite classically entangled light. *Light Sci. Appl.* **10**, 1-10 (2021).
26. Wang, J. et al. Terabit free-space data transmission employing orbital angular momentum multiplexing. *Nat. Photon.* **6**, 488-496 (2012).
27. Bahari, B. et al. Photonic quantum Hall effect and multiplexed light sources of large orbital angular momenta. *Nat. Phys.* **17**, 700-703 (2021).
28. Fang, X. et al. High-dimensional orbital angular momentum multiplexing nonlinear holography. *Adv. Photon.* **3**, 015001 (2021).
29. Hatano, N. & Nelson, D. R. Localization transitions in non-Hermitian quantum mechanics. *Phys. Rev. Lett.* **77**, 570 (1996).
30. Longhi, S. Non-Hermitian gauged topological laser arrays. *Ann. Phys.* **530**, 1800023 (2018).
31. Yu, Y., Jung, M. & Shvets, G. Zero-energy corner states in a non-Hermitian quadrupole insulator. *Phys. Rev. B* **103**, L041102 (2021).
32. McMaster, W. H. Polarization and the Stokes parameters. *Am. J. Phys.* **22**, 351-362 (1954).
33. Shen, Y. & Rosales-Guzmán, C. Nonseparable states of light: From quantum to classical. *Laser Photon. Rev.*, **2100533** (2022).
34. Lo, H.-K., Ma, X. & Chen, K. Decoy state quantum key distribution. *Phys. Rev. Lett.* **94**, 230504 (2005).
35. Ding, Y. et al. High-dimensional quantum key distribution based on multicore fiber using silicon photonic integrated circuits. *npj Quantum Inf.* **3**, 1-7 (2017).
36. Kagalwala, K. H., Di Giuseppe, G., Abouraddy, A. F. & Saleh, B. E. Bell's measure in classical optical coherence. *Nat. Photon.* **7**, 72-78 (2013).

37. Töppel, F., Aiello, A., Marquardt, C., Giacobino, E. & Leuchs, G. Classical entanglement in polarization metrology. *New J. Phys.* **16**, 073019 (2014).
38. Ndagano, B. et al. Characterizing quantum channels with non-separable states of classical light. *Nat. Phys.* **13**, 397-402 (2017).
39. Qian, X.-F., Little, B., Howell, J. C. & Eberly, J. Shifting the quantum-classical boundary: theory and experiment for statistically classical optical fields. *Optica* **2**, 611-615 (2015).
40. Bogaerts, W. et al. Programmable photonic circuits. *Nature* **586**, 207-216 (2020).

## Figure Legends

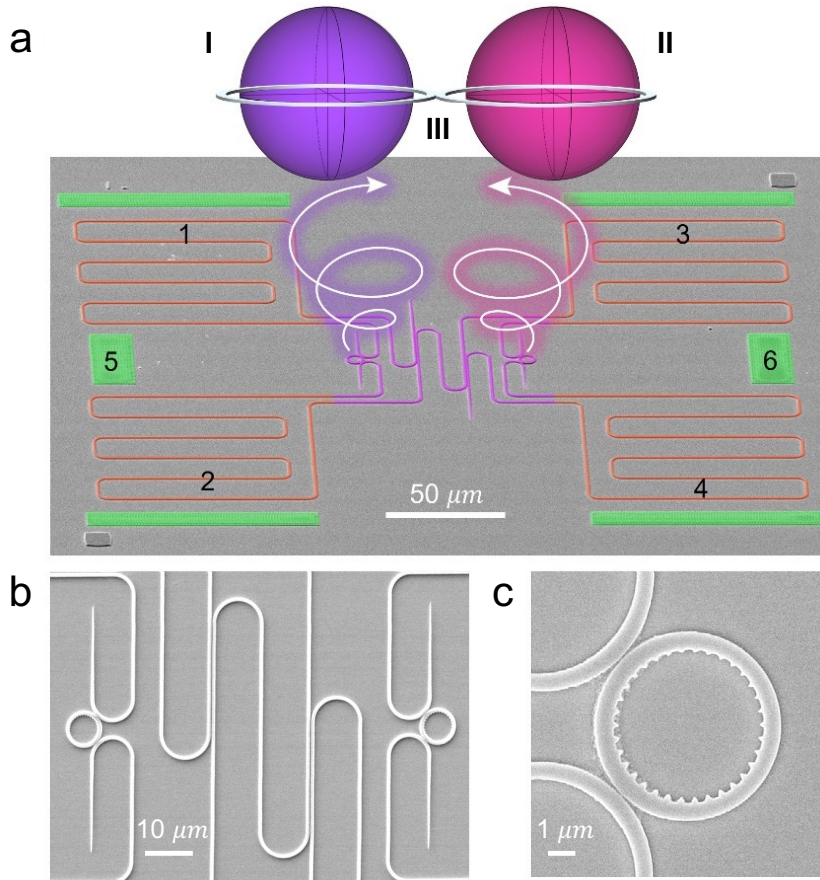


**Figure 1. The hyperdimensional spin-orbit microlaser.** **a**, Scanning electron microscope (SEM) image of the microlaser fabricated on an InGaAsP multiple quantum well platform, where two microring lasers are coupled through two 3 dB directional couplers (violet), four control waveguides (red), and alongside six heating pads (green). Note that control waveguides 1-4 are paired with their adjacent heating pads 1-4. The strength and phase of the coupling are determined by selective nanosecond pulsed optical pumping on each control waveguide 1-4 for active gain control and continuous-wave optical pumping on its adjacent heating pad 1-4 for thermally induced phase tuning. Heating pads 5 and 6 are implemented to manipulate the frequency detuning between two microring lasers. With strategically designed angular gratings, emissions from two microlasers feature two pairs of spin-orbit-coupled vectorial states, each covering a distinguished HOPS. The coupling between two microrings leads to the coupling between two generated HOPS, forming a Bloch hypersphere defining an  $SU(4)$  symmetry in a 4D Hilbert space. **b**, SEM image of the 3 dB directional coupler. **c**, SEM image of the right microring laser with the angular grating inscribed

on the inner side wall. The diameter of the microrings is 7  $\mu\text{m}$  and the width of the waveguide is 650 nm. With the orders of angular gratings being 30/34 for left/right microrings, their emitted vector beams carry spin-orbit-coupled states of  $|+/-2, \uparrow/\downarrow\rangle$  and  $| -/+2, \uparrow/\downarrow\rangle$ , respectively.

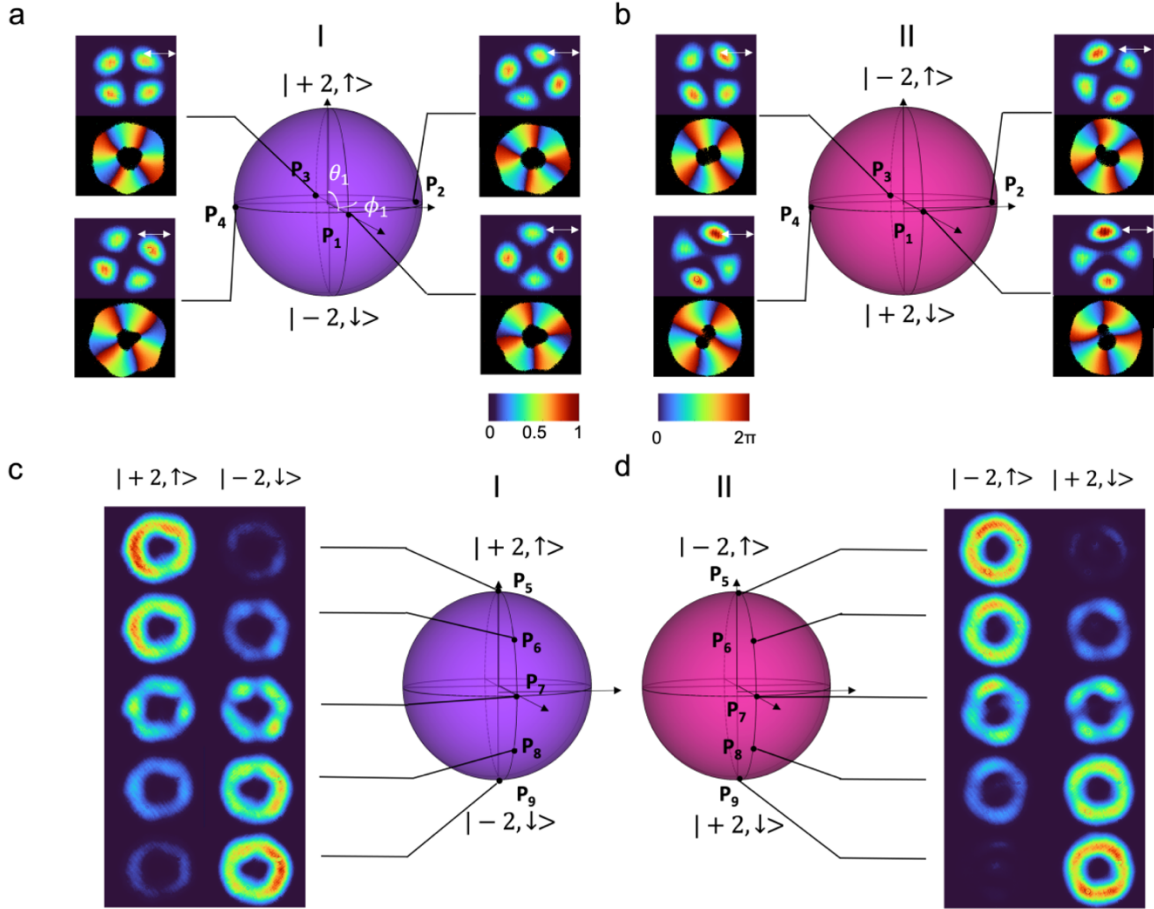


**Figure 2. Independent emission control on two distinguished HOPS.** **a**, Phase tuning on HOPS **I** with two pole states defined as  $|N_I\rangle = |+2, \uparrow\rangle$  and  $|S_I\rangle = |-2, \downarrow\rangle$ . The relative phase between two pole states can be dynamically tuned via heating pads 1 and 2, winding along the equator in the azimuthal direction as demonstrated by 4 special states with an equal phase difference of  $\pi/2$ . The upper panel in each rectangle shows captured emission pattern after a horizontally placed linear polarizer, whereas the lower panel maps the measured relative phase between two pole states, both rotating in the same manner with  $(\varphi_2 - \varphi_1)/4$ . **b**, Phase tuning on HOPS **II** with two pole states defined as  $|N_{II}\rangle = |-2, \uparrow\rangle$  and  $|S_{II}\rangle = |+2, \downarrow\rangle$ , where the relative phase between two pole states is dynamically tuned via heating pads 3 and 4, rotating with  $(\varphi_3 - \varphi_4)/4$ . **c**, Chiral

control between  $|N_I\rangle$  and  $|S_I\rangle$  on HOPS **I**, enabled by controlled pumping on control waveguides 1 and 2 in Fig. 1a. Five special states are characterized, where the intensities of the two spin components  $|+2, \uparrow\rangle$  (left) and  $|-2, \downarrow\rangle$  (right) are separately measured, revealing the amplitude ratios between two pole states and thus the state evolution from  $|N_I\rangle$  to  $|S_I\rangle$ . **d**, Chiral control between  $|N_{II}\rangle$  and  $|S_{II}\rangle$  on HOPS **II**, enabled by controlled pumping on control waveguides 3 and 4 in Fig. 1a. Five special states are characterized, where the intensities of the two spin components  $|-2, \uparrow\rangle$  (left) and  $|+2, \downarrow\rangle$  (right) are separately measured, revealing the state evolution from  $|N_I\rangle$  to  $|S_I\rangle$ .

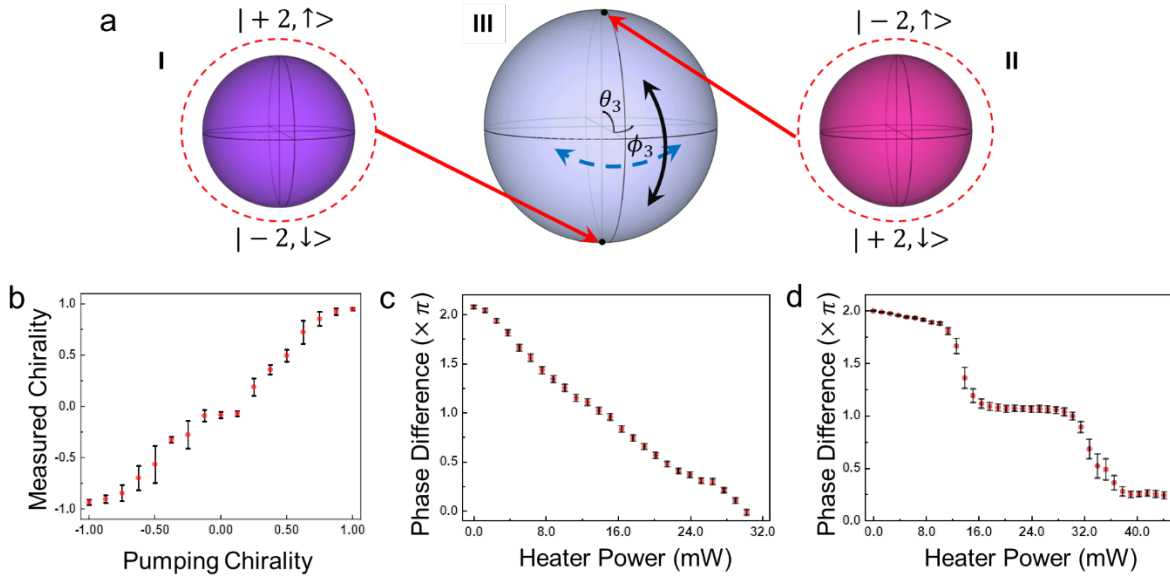


**Figure 3. SU(4) Bloch hypersphere by delicate control of inter-ring coupling.** **a**, Schematic of the formation of a Bloch hypersphere and the SU(4) state control of laser emission. The states on the SU(4) Bloch hypersphere can be represented on a nested HOPS **III**: Because of intrinsic orthogonality between these two HOPSs, two arbitrary pole states can be selected for HOPS **III**, one from each HOPS (**I** or **II**) and constituting a complete 4D Hilbert space. SU(4) state control is completed on HOPS **III** by adjusting two DOFs between the two microrings: their relative amplitude and phase, corresponding to state tuning along the latitude and longitude, respectively. **b**, Measured chirality control on HOPS **III** from its south pole to north pole by differential pumping of two microrings. Pumping chirality is defined as  $(P_I - P_{II})/(P_I + P_{II})$ , where  $P_{I,II}$  denotes optical pumping power on the left/right ring. Measured chirality is given by  $(I_I - I_{II})/(I_I + I_{II})$ , where  $I_{I,II}$  is the intensity of laser emission from the left/right ring. **c** and **d** show

phase control to move the state along the latitude of HOPS **III** as a function of the power of the continuous-wave laser applied on heater 5: in **c**, state  $0.9851|+2, \uparrow\rangle + 0.1719e^{0.550\pi i}| - 2, \downarrow\rangle$  (at  $\theta_1 = 0.11\pi$ ,  $\phi_1 = 0.55\pi$ ) on HOPS **I** and state  $0.4540| - 2, \uparrow\rangle + 0.8910e^{1.260\pi i}| + 2, \downarrow\rangle$  (at  $\theta_2 = 0.70\pi$ ,  $\phi_2 = 1.26\pi$ ) on HOPS **II** are selected, showing a linear phase variation, whereas in **d**, state  $0.7705|+2, \uparrow\rangle + 0.6374e^{1.940\pi i}| - 2, \downarrow\rangle$  at ( $\theta_1 = 0.44\pi$ ,  $\phi_1 = 1.94\pi$ ) on HOPS **I** and state  $0.6613| - 2, \uparrow\rangle + 0.7501e^{0.230\pi i}| + 2, \downarrow\rangle$  at ( $\theta_2 = 0.54\pi$ ,  $\phi_2 = 0.23\pi$ ) on HOPS **II** are selected, showing a step-like phase variation on HOPS **III** attributed to supermode hopping.

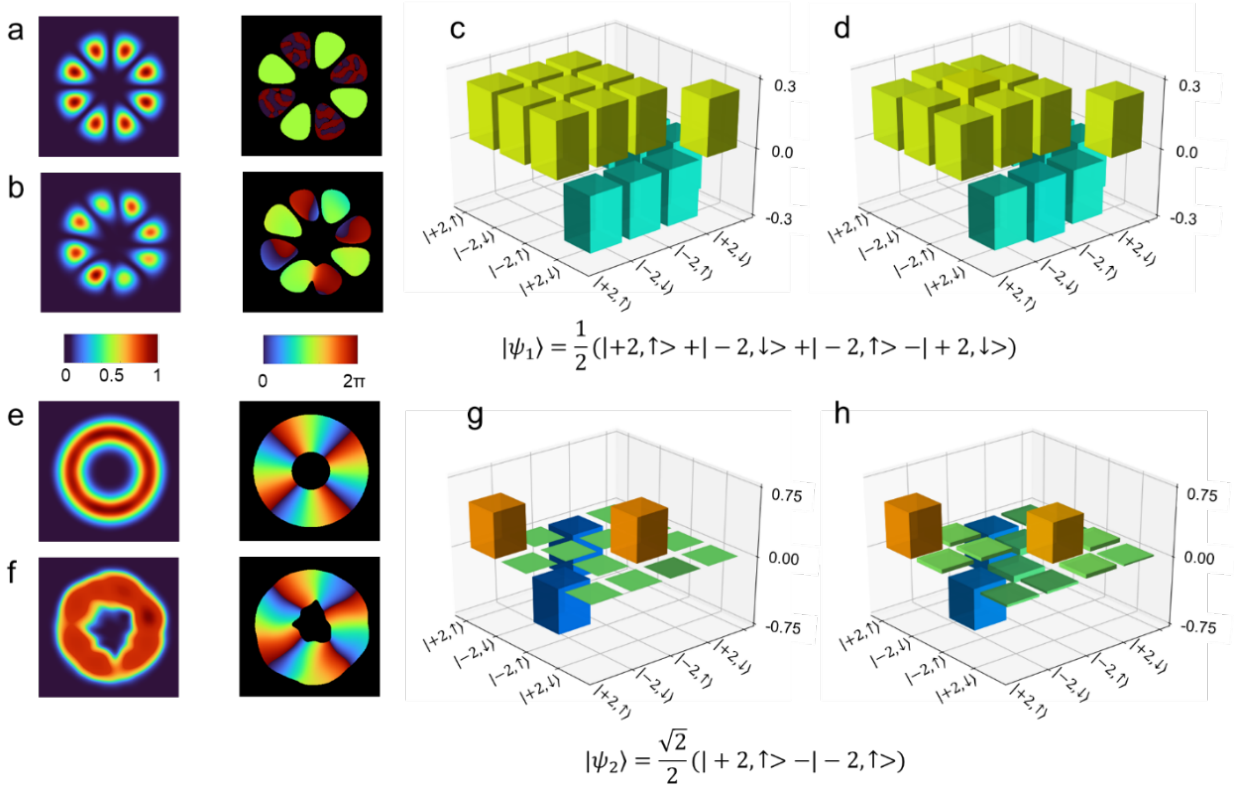


**Figure 4. Generation and reconfiguration of SU(4) states.** **a-d**, Characterization of a high-dimensional superposition state  $|\psi_1\rangle = \frac{1}{2}(|+2, \uparrow\rangle + | - 2, \downarrow\rangle + | - 2, \uparrow\rangle - | + 2, \downarrow\rangle)$ , when equally pumping two microring lasers and 4 control waveguides but selectively conducting the temperature difference between heating pads 3 and 4 appropriately. **a** shows theoretical results of cross-correlation far-field intensity and phase patterns that capture the vectorial nature of  $\psi_1$ . **b** displays the corresponding experimentally reconstructed patterns, after image processing to select only the AC component in raw data. **c** and **d** are theoretically calculated vs. experimentally retrieved density matrix of  $\psi_1$ , respectively, featuring fidelity of 0.998. **e-h**, Same as **a-d** but for



$|\psi_2\rangle = \frac{\sqrt{2}}{2}(|+2, \uparrow\rangle - |-2, \uparrow\rangle)$ , generated by equally pumping two microring lasers but selectively pumping only control waveguides 1 and 4 and thermally tuning heating pad 5 appropriately. **e** and **f** capture the non-vectorial nature of  $|\psi_2\rangle$ . **h** shows experimental fidelity of 0.942 when compared with **g**.

## Methods

### Design of the microring cavity for spin-orbit emission

The geometry of the cross-section of the microring resonator (600 nm wide and 200 nm thick) is designed to enable spin-orbit locking: left-hand ( $\uparrow$ : spin-up with  $s = +1$ ) or right-hand ( $\downarrow$ : spin-down with  $s = -1$ ) polarization in the evanescent tail of guided mode is locked to only one chiral mode (either CW or CCW)<sup>1,2,41,42</sup>. The diameter of the microrings is 7  $\mu\text{m}$ , thereby supporting a whispering gallery mode with azimuthal order  $N = 33$  at the lasing wavelength of approximately 1538 nm. Two sets of angular gratings with different orders  $M = 30/34$  are inscribed on the inner sidewall of the left and right microrings (Fig. 1c), respectively, leading to the total angular momentum for extracted laser emission:  $J = l + s = C(N - M) = \pm 3/\mp 1$ , where  $C = \pm 1$  for CCW and CW modes, respectively. In other words, the spin-orbit locked states  $|l, s\rangle$  in the left ring are  $|+2, \uparrow\rangle$  (CW) and  $|-2, \downarrow\rangle$  (CCW), whereas those in the right ring are  $|-2, \uparrow\rangle$  (CW) and  $|+2, \downarrow\rangle$  (CCW). The OAMs of the four eigen states are designed to carry the same topological charge (i.e.,  $\pm 2$ ) to ensure their perfect spatial overlap in the far-field. As a result, a 4D Hilbert space and its associated SU(4) Bloch hypersphere are formed by arbitrary coherent superpositions of the laser emission from these two microrings in free space.

### Sample fabrication

The device was fabricated using standard nanofabrication techniques based on electron beam lithography. Hydrogen silsesquioxane (HSQ) solution in methyl isobutyl ketone (MIBK) was used as a negative electron beam lithography resist. The concentration ratio of HSQ (FOX15) and MIBK was adjusted such that after exposure and development the resist was sufficiently thick as an etching mask for subsequent dry etching. The resist was then soft-baked, and the structure was patterned by electron beam exposure. Electrons convert the HSQ resist to an amorphous oxide. The patterned wafer was then immersed and slightly stirred in the tetramethylammonium hydroxide (TMAH) solution (MFCD-26) for 120 seconds and rinsed in de-ionized water for 60 seconds. The exposed and developed HSQ pattern served as a mask for the subsequent inductively coupled plasma etching process that uses  $\text{BCl}_3$ :Ar plasma with a gas ratio of 15 : 5 sccm, respectively, with RF power of 50 W and ICP power of 300 W under a chamber pressure of 5 mT. After dry etching, HSQ resist was removed by immersing the sample in buffered oxide etchant (BOE). To overcome potential ring-to-ring non-uniformity at the nanoscale across the whole

device due to fabrication imperfection, the sample was covered with a cladding layer of  $\text{Si}_3\text{N}_4$  using plasma enhanced chemical vapor deposition to enhance the evanescent coupling strengths to ensure relatively high coupling despite slight frequency detuning. The wafer was then bonded to a glass slide which functions as a holder. Finally, the InP substrate was removed by wet etching with a mixture of HCl (Hydrochloride acid) and  $\text{H}_3\text{PO}_4$  (Phosphoric acid)

### **Experimental setup and characterizations of the lasing spectrum and OAM order**

The fabricated sample is characterized using the optical setup shown in Extended Data Fig. 1a with respect to its lasing wavelength, OAM, and the control on HOPS. The microlaser is pumped from the backside by a nanosecond pulsed laser with a 10 kHz repetition rate and 8 ns duration at a wavelength of 1064 nm. The pulsed pumping light is shaped by a spatial light modulator and imaged onto the sample through a 4- $f$  demagnification system and its intensity is controlled by using a combination of a half waveplate and a polarization beam splitter. A continuous wave laser at 1064 nm for heating is focused onto the sample by the same 10 $\times$  microscope objective with a numerical aperture (NA) of 0.28 used in the 4- $f$  demagnification system. Its power is directly controlled by its pumping current. The laser emission from the front side was collected by a 20 $\times$  microscope objective (NA = 0.42) and guided into a monochromator for the spectral analysis. The beam was passed through a spatial filter on demand for beam selection (i.e., a pinhole at the image plane to observe the emission from either the left ring, the right ring, or both) and later passed through a linear polarizer with 0, 45, 90 and 135 degrees to the vertical direction and a combination of a linear polarizer and quarter wave plate into an imaging system to conduct the Stokes polarimetry (see Methods Section: Stokes polarimetry: Relative phase measurement). Additionally, a cylindrical lens is used to characterize the OAM nature of the emission. Extended Data Fig. 1b and c shows the measured lasing spectrum from the microlaser (Extended Data Fig. 1b) and the light-light curve where the kink corresponds to the onset of laser action (i.e., laser threshold) (Extended Data Fig. 1c).

The OAM nature of emissions from the spin-orbit microlaser is verified by using a cylindrical lens which performs a 1D Fourier transform of the input beam<sup>3</sup>. The value of OAM charge can be determined by counting the number of dark lines in the measured patterns through the cylindrical lens while the sign of the OAM charge corresponds to the direction of the dark lines.

The results confirmed the chiral control via selective pumping of the nanosecond laser (Extended Data Fig. 2).

Extended Data Fig. 2a shows laser emission from the left microring and its chiral control on HOPS I. In the scenario where all the control waveguides except waveguide 2 are pumped, we reach the condition of  $g_1 \gg g_2$ , which leads to the excitation of only state  $|N_I\rangle = | + 2, \uparrow \rangle$  on HOPS I. The captured image (unpolarized) shows fringe patterns with two dark lines pointing to the top right corner, confirming the OAM charge of emission to be +2. The polarization state of emission can be verified by using a combo of a quarter waveplate and a linear polarizer, showing only the left-handed circular polarization (i.e., spin-up:  $\uparrow$ ). If all the control waveguides are equally pumped (i.e.,  $g_1 = g_2$ ), laser emission becomes a superposition of  $|N_I\rangle = | + 2, \uparrow \rangle$  and  $|S_I\rangle = | - 2, \downarrow \rangle$ , moving to the equator on HOPS I. Without the selection of polarizations, there is no clear dark line, indicating no net OAM. However, if we selectively extract only the left circular polarization component (i.e., spin-up:  $\uparrow$ ), the fringe pattern shows two dark lines pointing to the top right corner, suggesting the OAM charge to be +2; on the other hand, if only the right circular polarization (i.e., spin-down:  $\downarrow$ ) component is selected, the fringe pattern shows two dark lines pointing to the top left corner, manifesting the OAM charge to be  $-2$ . If only waveguide 1 is selectively unpumped, we reach the condition of  $g_2 \gg g_1$ , which yields the excitation of only state  $|S_I\rangle = | - 2, \downarrow \rangle$  on HOPS I. Consequently, the unpolarized image is consistent with the spin-down image, showing the intrinsic right-hand circular polarization of emission. The fringe pattern also shows two dark lines pointing to the top left corner, validating the OAM charge of  $-2$ .

Similarly, Extended Data Fig. 2b shows laser emission from the right microring and its chiral control on HOPS II. If all the control waveguides except waveguide 3 are pumped, the condition is  $g_4 \gg g_3$ , corresponding to the excitation of only state  $|N_{II}\rangle = | - 2, \uparrow \rangle$  on HOPS II. In this case, the fringe pattern shows two dark lines pointing to the top left corner and contains only the spin-up component. At the condition of  $g_3 = g_4$  when all the waveguides are equally pumped, the unpolarized image shows zero net OAM with its spin up component corresponding to  $|N_{II}\rangle = | - 2, \uparrow \rangle$  and its spin-down component being  $|S_{II}\rangle = | + 2, \downarrow \rangle$ , as suggested by the opposite orientations of the two dark lines in the fringe patterns. If  $g_3 \gg g_4$ , we observe only the spin-down component with the OAM charge of +2, verifying the successful excitation of only  $|S_{II}\rangle = | + 2, \downarrow \rangle$ .

Moreover, the chirality of emission on each HOPS (i.e., the latitude of the HOPS) can be systematically controlled by pumping different control waveguides with different power. Here, we define the pumping chirality as  $(P_1 - P_2)/(P_1 + P_2)$  for HOPS **I** and  $(P_4 - P_3)/(P_4 + P_3)$  for HOPS **II**, where  $P_i$  is the pumping power applied on control waveguide  $i$ . The chirality of the emission can be defined as  $C = (I_\uparrow - I_\downarrow)/(I_\uparrow + I_\downarrow)$ , where intensity of each component can be conveniently measured by polarization filtering to select only the right spin. The experimentally measured chirality control of both microrings can be seen in Extended Data Fig. 3. Note that three different conditions on each ring as shown in Extended Data Fig. 2 correspond to emission chirality of +1, 0, and -1.

### Stokes polarimetry: Relative phase measurement

Each individual HOPS represents the superposition of two spin-orbit-coupled states, where the latitude corresponds to the chirality between the two states, while the longitude is related to the relative phase between them. Since the two spin-orbit-coupled states carry opposite spins, their relative phase  $\phi(x, y)$  at an arbitrary point on a HOPS can be retrieved using the Stokes polarimetry<sup>32</sup>:  $\phi(x, y) = \text{atan} 2(S_2, S_1) + \pi$ , where  $S_1 = I_0(x, y) - I_{90}(x, y)$  and  $S_2 = I_{45}(x, y) - I_{135}(x, y)$ , and as  $I_0(x, y)$ ,  $I_{45}(x, y)$ ,  $I_{90}(x, y)$ ,  $I_{135}(x, y)$  are intensities of linear polarization states at  $0^\circ$ ,  $45^\circ$ ,  $90^\circ$ ,  $135^\circ$ . For example, Extended Data Fig. 4 shows the intensity distribution of six difference polarization states of emission from the left microring at **P**<sub>2</sub> on HOPS **I** (Fig. 2a), including 4 linear polarization states of  $0^\circ$ ,  $45^\circ$ ,  $90^\circ$ ,  $135^\circ$  and 2 circular polarization states of spin  $\uparrow$  and  $\downarrow$ .

Similar to the chiral control shown in Extended Data Fig. 3, selectively exciting heaters 1-4 using the continuous-wave laser can introduce an active phase tuning scheme to move the state in the latitude of the HOPS. Extended Data Fig. 5 shows the experimental demonstration of the control of the phase in the two individual HOPS (**I** and **II**) as a function of power difference of the laser beam applied on two pairs of heaters 1/2 and 3/4, respectively.

### Frequency detuning between two microring lasers

Frequency detuning  $g_r$  and gain/loss contrast  $g_i$  between two microring lasers provide two extra knobs to control the 4D state in the Bloch hypersphere. Although  $g_i$  can be performed by controlling the power difference between nanosecond laser applied on the two microrings,  $g_r$  is

conducted by exciting either heating pad 5 or 6. Extended Data Fig. 6 shows the on-site frequency detuning between the two microrings as a function of the power of the continuous-wave laser applied on heating pad 5. In this experiment, only the two microrings are pumped by the nanosecond laser, while all four control waveguides are not. In this manner, the two microrings are uncoupled, so we can accurately measure their own resonant wavelengths from their respective lasing spectra and then determine the wavelength difference. Note that red shifts are observed for the resonant wavelengths of both microrings as the heating power increased, arising from the thermo-optical effect.

### **Method References:**

41. Bliokh, K. Y., Rodríguez-Fortuño, F. J., Nori, F. & Zayats, A. V. Spin-orbit interactions of light. *Nat. Photon.* **9**, 796-808 (2015).
42. Van Mechelen, T. & Jacob, Z. Universal spin-momentum locking of evanescent waves. *Optica* **3**, 118-126 (2016).

**Acknowledgements:**

We acknowledge the support from the U.S. Army Research Office (ARO) (W911NF-19-1-0249 and W911NF-21-1-0148), National Science Foundation (NSF) (ECCS-1932803, ECCS-1842612, OMA-1936276, and PHY-1847240), Office of Naval Research (ONR) (N00014-20-1-2558), and King Abdullah University of Science & Technology (OSR-2020-CRG9-4374.3). L.F. also acknowledges the support from Sloan Research Fellowship. This work was partially supported by NSF through the University of Pennsylvania Materials Research Science and Engineering Center (MRSEC) (DMR-1720530) and carried out in part at the Singh Center for Nanotechnology, which is supported by the NSF National Nanotechnology Coordinated Infrastructure Program under grant NNCI-1542153.

**Author Contributions**

Z.Z., H.Z. and L.F. designed the experiment. H.Z., Z.Z. and L.F. developed the concept on the high-dimensional states. L.G. Z.Z., H.Z., S.L. and L.F. constructed the theoretical model. Z.Z., H.Z., T.W., and Z.G. conducted numerical simulations. X.Q., T.W., and H.Z. fabricated the samples. Z.Z., H.Z., S.W. and T.W. performed the measurements and data processing. All authors contributed to discussions and manuscript preparation.

**Author Information:****Corresponding author**

Correspondence to Liang Feng ([fenglia@seas.upenn.edu](mailto:fenglia@seas.upenn.edu)).

**Competing Interests**

The authors declare no competing interests.

**Data availability statement:**

The data represented in Fig. 3b-d are available as Source Data. All other data that support the plots within this paper and other findings of this study are available from the corresponding author upon reasonable request.



**Code availability statement:**

The computer codes that support the plots within this paper and other findings of this study are available from the corresponding author upon reasonable request.

## Extended Figure Legends

**Extended Data Figure 1. Optical setup and spectral characterization of the microlaser.** **a**, Optical setup for the characterization of the microlaser. **b**, Lasing spectrum of the microlaser under a pumping intensity of  $25 \text{ kW/cm}^2$  which shows a robust single mode lasing. **c**, Light-light curve of the microlaser.

**Extended Data Figure 2. Chiral control and OAM characterization of spin-orbit-coupled emissions from two microrings by a cylindrical lens.** **a**, Characterization of OAM emissions from the left microring under different pumping and measurement conditions ( $g_1 \gg g_2$ ,  $g_1 = g_2$ , and  $g_2 \gg g_1$ ). **b**, Characterization of OAM emissions from the right microring under different pumping and measurement conditions ( $g_4 \gg g_3$ ,  $g_3 = g_4$ , and  $g_3 \gg g_4$ ). In both **a** and **b**, top, middle and bottom rows show unpolarized, left-handed polarized, and right-handed polarized components of laser emission.

**Extended Data Figure 3. Experimental demonstration of chiral control on HOPS I and II.** **a**, HOPS I and **b**, HOPS II.

**Extended Data Figure 4. Stoke polarimetry to retrieve the relative phase between two pole states on HOPS.** **a**, Six polarization states are recorded corresponding to  $I_0(x, y)$ ,  $I_{45}(x, y)$ ,  $I_{90}(x, y)$ ,  $I_{135}(x, y)$ ,  $I_{\uparrow}$ , and  $I_{\downarrow}$  for phase retrieval using the Stokes polarimetry. White arrows denote the direction of polarizations. **b**, The retrieved relative phase distribution between  $|+2, \uparrow\rangle$  and  $|-2, \downarrow\rangle$  components, showing  $8\pi$  phase winding in the azimuthal direction.

**Extended Data Figure 5. Experimental phase tuning in two individual HOPS associated with the left and right microrings.** **a**, Phase tuning on HOPS I associated with the left microring ( $\phi = \varphi_2 - \varphi_1$ ) under continuous-wave laser heating. Positive/negative heating power here represents heating on heater 1/2, respectively. **b**, Phase tuning on HOPS II associated with the right microring ( $\phi = \varphi_3 - \varphi_4$ ) under continuous-wave laser heating. Positive/negative heating power here represents heating on heater 3/4, respectively. The slight difference in slopes in both panels results from small variance in absorption efficiency associated with different heaters.

**Extended Data Figure 6. Controlled frequency detuning in the microlaser.** The frequency detuning between the two microrings under different heating power from the continuous-wave laser, showing the increase of the detuning as the increase of heater power.